



**HAL**  
open science

# Patterns of Glacial Deformation in a Lobate Debris Apron: Implications for Glacial Geology, Internal Structure, and Regional Climate History

A Grau Galofre, J K Serla, P Becerra, A Noblet, Susan J. Conway

► **To cite this version:**

A Grau Galofre, J K Serla, P Becerra, A Noblet, Susan J. Conway. Patterns of Glacial Deformation in a Lobate Debris Apron: Implications for Glacial Geology, Internal Structure, and Regional Climate History. *Planetary and Space Science*, 2022, 10.1016/j.pss.2022.105548 . hal-03851125v2

**HAL Id: hal-03851125**

**<https://hal.science/hal-03851125v2>**

Submitted on 12 Sep 2023

**HAL** is a multi-disciplinary open access archive for the deposit and dissemination of scientific research documents, whether they are published or not. The documents may come from teaching and research institutions in France or abroad, or from public or private research centers.

L'archive ouverte pluridisciplinaire **HAL**, est destinée au dépôt et à la diffusion de documents scientifiques de niveau recherche, publiés ou non, émanant des établissements d'enseignement et de recherche français ou étrangers, des laboratoires publics ou privés.

# Patterns of martian glacial deformation: implications for glacio-geology, internal structure, and regional climate

Anna Grau Galofre<sup>\*1</sup>, Jayanth K. Serla<sup>1</sup>

*School of Earth and Space Exploration, Arizona State University. 781 Terrace Mall,  
Tempe, AZ 85287*

Patricio Becerra<sup>1</sup>

*Space Research and Planetary Sciences, Physikalisches Institut, Universität Bern,  
Gesellschaftsstrasse 6, CH-3012 Bern Switzerland*

Axel Noblet<sup>1</sup>, Susan J. Conway<sup>1</sup>

*Nantes Université, Université d'Angers, Le Mans Université, CNRS UMR 6112 Laboratoire  
de Planétologie et Géosciences, Bât. 4, 2 rue de la Houssinière, 44322 Nantes, France*

---

## Abstract

Viscous Flow Features (VFF) are widespread in the martian mid-latitudes and indicative of near-surface ice deposits. Their distribution and morphology hint at the regional history of ice deposition and ablation, as well as changes in surface temperature. Here we interrogate the deformation history of a type of VFF, a Lobate Debris Apron (LDA), located in the eastern Hellas region from its surface morphology, discussing the implications it poses for its internal structure and regional climate variability. Our observations integrate data from the Colour and Stereo Surface Imaging System (CaSSIS), the SHallow RADar (SHARAD), the Context Camera (CTX), the High Resolution Imaging Science Experiment (HiRISE), and the Mars Orbiter Laser Altimeter (MOLA). Morphological observations, spectral analysis of characteristic wavelengths, and ice deformation stability analysis place constraints on the dynamics and deformation history of the deposit. We discuss contrasting hypotheses for the origin

---

<sup>\*</sup>Corresponding author

*Email address:* [anna.graugalofre@univ-nantes.fr](mailto:anna.graugalofre@univ-nantes.fr) (Susan J. Conway )

of the different surface structures, including the possibility of gelifluction in addition to glacial creep. Our results provide a guide to interpret glacial deformation patterns in martian VFFs in the light of internal structure, regional climate history, and underlying topography.

*Keywords:* CaSSIS, Amazonian glaciation, Lobate Debris Aprons (LDA), Mars

---

## 1. Introduction

The flow and deformation of ice-rich material is an important agent of Amazonian (last 3 Gyr) landscape modification in the martian mid-latitudes [1, 2, 3]. Ice deposits on Mars are true time capsules [4, 5]. Their stratigraphy records the history of mass balance since their emplacement, their deformation structures reflect the balance of forces applied [6], the associated landforms may indicate the existence of past liquid water [7], and their presence opens the door to future human in-situ resource utilization (ISRU). Characterizing the origin and evolution of such features through their morphology is important to understand the glacial, geological, and climate history of Amazonian Mars.

Ice-rich landforms are commonly grouped in four types [e.g., 8]: Glacier-like forms (GLF) [9, 10, 11]; Lobate Debris Aprons (LDA) [12, 13, 14, 15]; Concentric Crater Fills (CCF) [16, 12, 2]; and Lineated Valley Fills (LVF) [17, 16]. The last three types are larger ( $\sim 10$ -100 km) and are dated throughout the Amazonian period encompassing 3 to  $<1$  Gyr ago [18, 11], whereas GLFs are smaller ( $\sim 15$  km) and generally more recent [19, 11], possibly recording recent episodes of glaciation on Mars.

Data from the Shallow Radar (SHARAD) instrument demonstrated that LDAs [2] are deposits of massive glacial ice covered by a debris layer of unknown thickness [14, 13, 20]. However, ice mass-balance and deformation history, as well as thickness and internal deposit structure are still matters of debate. The objective of this manuscript is to characterize the deformation patterns and history of an LDA located in the eastern Hellas region.

Our work also serves as a case study for the use and integration of CaSSIS  
25 data with existing datasets, including CTX, SHARAD, and MOLA/HRSC, for  
the detailed examination of icy deposits. Using CaSSIS, we describe the high  
resolution morphometry and the deformation patterns of the target. To inter-  
rogate the glacio-geological history of the deposit, we make use of CaSSIS BLU  
(blue) and PAN (visible) color bands [21, 22], a Color Band Ratio Compos-  
30 ite (CBRC), topography from the Mars Orbiter Laser Altimeter (MOLA, Mars  
Global Surveyor MGS) [23] and HRSC (High Resolution Stereo Camera, Mars  
Express) [24] and stereo-derived topography from CTX [25] (Mars Reconnaissance  
Orbiter, MRO), images from the High Resolution Imaging Experiment  
(HiRISE, MRO) [26], and data from SHallow RADar (SHARAD, MRO) [27].

### 35 *1.1. Overview of the area of interest: Lower Reull Vallis*

Eastern Hellas encompasses a rich geological history [e.g., 28, 29, 30, 31, 32,  
33], with a notable presence of icy landforms (figure 1). Large fractions of Reull  
Vallis are covered in LVF [e.g., 12, 29, 34, 35, 30, 8, 2], and the plains surrounding  
Reull contain multiple examples of CCFs and LDAs [35, 30, 15]. Nearly 200  
40 GLFs have been identified in this area so far [36], as shown in figure 1. Our  
LDA of interest is located at  $41.06^{\circ}\text{S}$ ,  $101.04^{\circ}\text{E}$  occupying the cross-section of  
Reull Vallis as shown in figure 1 [37, 29, 35, 30, 33].

### *1.2. Structure of the manuscript*

In section 2, we describe the main datasets considered in this study: CaSSIS,  
45 SHARAD, CTX, and MOLA/HRSC. In section 3 we present the key observa-  
tions in the context of the existing literature, analyzing topography, morphology  
and morphometry, and presence of ice on and under the surface. In the discus-  
sion (section 4) we integrate all results with models of glacial deformation to  
interrogate the origin and evolution of this LDA. We finally present our conclu-  
50 sions in section 5.

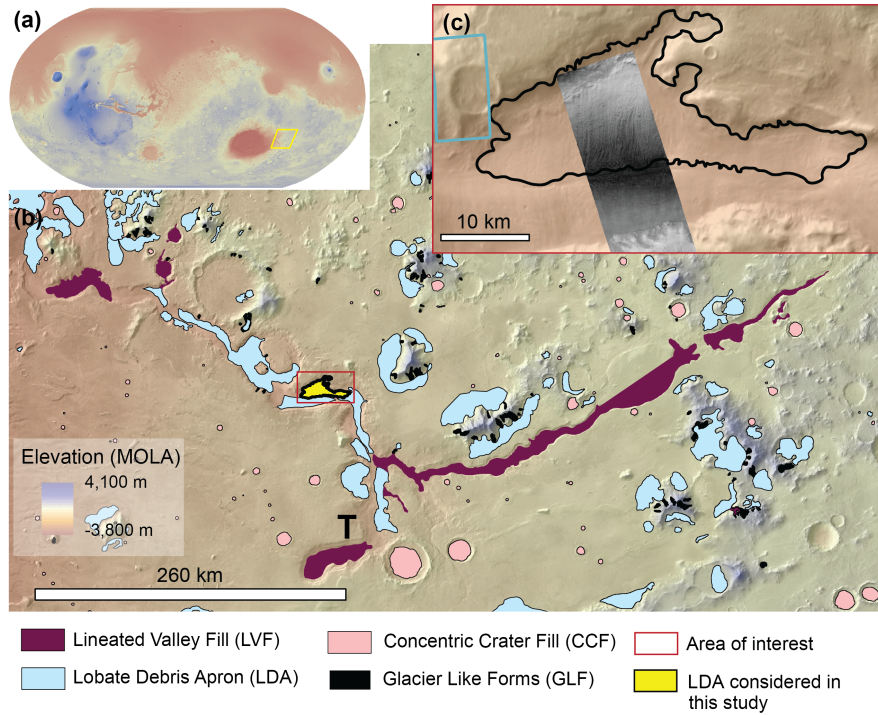


Figure 1: Location and context for our area of study. (a) Global map of Mars (MOLA/HRSC) showing Lower Reull Vallis in a yellow box. (b) Lower Reull Vallis region (MOLA/THEMIS) with previously mapped icy features [15, 36] and our area of interest bounded by a red box. (c) Zoomed in view of the LDA of interest, showing MOLA/HRSC underlain by CTX data and overlain by CaSSIS (black and white image), with blue box locating HiRISE image ESP\_049593.1390\_RED. MOLA/HRSC: DLR, NASA, Goddard Space Flight Center, USGS; THEMIS IR daytime (v12): NASA/JPL-Caltech/Arizona State University. CaSSIS: ESA/Roscosmos/CaSSIS/Uni Bern.

## 2. Datasets

### 2.1. *CaSSIS*

The Colour and Stereo Surface Imaging System (CaSSIS) is the main imaging system on board of the ExoMars Trace Gas Orbiter (TGO) mission [21].  
55 CaSSIS is a full-swath color stereo image system with a resolution of  $< 5$  m/pixel and a footprint of  $9.4 \times 50$  km. Color/spectral capabilities of CaSSIS come in four bands [21, 22]: A blue-green band (BLU) at 499.9 nm (bandwidth 118.0 nm), an orange-red broadband (PAN) at 675 nm (bandwidth 229.4 nm), a red band (RED) at 836.2 nm (bandwidth 94.3 nm), and a near infrared band (NIR)  
60 at 936.7 nm (bandwidth 113.7 nm) [22].

We use CaSSIS data for two purposes. First, to examine the morphology and morphometry of the Lower Reull Vallis cross-section at a high spatial resolution, with lower Signal to Noise (STN) ratios than CTX (100 [21] vs. 66 [38]). Second, we use the CaSSIS BLU band to assess whether surface or near surface ice is  
65 currently present. Ice or frost-bearing surfaces have high reflectance values over the entire 400-1100 nm sensitivity range of CaSSIS [39], and are more reflective in blue wavelengths when compared to other surface materials on Mars [22]. We combine the BLU and PAN bands to produce a Color Band Ratio Composite (CBRC) image:  $CBRC = [BLU - 4 \times PAN] / [4 \times PAN / BLU]$ , which we  
70 use to highlight surface features and examine their morphometry.

We work with CaSSIS image cube MY34\_005511.224\_0 as shown in figure 1 (also supplement). This cube includes the BLU and PAN color bands at a resolution of 4.6 m/pixel. The image is located within the first 150 km of the Lower Reull segment, oriented N-NW to S-SE and spanning most of Reull Vallis’  
75 cross-section.

### 2.2. *SHARAD*

The search for liquid or frozen water within the first kilometer of the martian subsurface is one of the main objectives of SHARAD. SHARAD is a remote, sub-surface sounding radar that transmits  $85\text{-}\mu\text{s}$  linear chirps at a central radio

80 frequency of 20 MHz [27]. It has a horizontal resolution of between 300 m and  
3 km, and a vertical resolution of 15 m in free space, which can translate to up  
to <10 m in the martian subsurface. The transmitted radar signal is reflected  
from the subsurface at interfaces that separate materials with different dielectric  
constants. Therefore, reflections contain information about material dielectric  
85 properties, roughness at the radar wavelength, and slope of the surface with  
respect to the spacecraft [40].

Naturally, subsurface reflections are particularly sensitive to large permit-  
tivity contrasts, as is the case with the presence of water ice in contact with  
solid rock. However, clutter caused by reflections from off-nadir surfaces like  
90 vallis walls can also cause increased power at time delays that may be similar  
to those caused by dielectric constant variations. To assess the extent of the  
clutter, we must compare SHARAD’s two-dimensional radar images (known as  
radargrams) to simulated clutter models derived from MOLA data [40], as is  
standard in the analysis of subsurface radar data.

95 We used six SHARAD observations (Product IDs: S\_00365901, S\_00878801,  
S\_01301401, S\_01700301, S\_03948601, S\_05716901) corresponding to our area  
of interest to investigate any subsurface reflectors, which could indicate the  
presence of water-ice or high-density bedrock in the subsurface.

### 2.3. MOLA/HRSC

100 We use the gridded, blended MOLA/HRSC elevation map (NASA/ MGS  
MOLA and ESA/ MEX/ HRSC) [41] at a nominal resolution of 200 m/pixel at  
the equator, in combination with individual MOLA altimetry points (horizontal  
footprint of 100 m, vertical resolution  $\pm 3$  m) [42], to attain an overview of the  
regional topography and cross-section at our site of interest.

### 105 2.4. CTX

The Context Camera (CTX) aboard the Mars Reconnaissance Orbiter (MRO)  
is aimed at providing detailed background information for high-resolution ob-  
servations of the martian surface. Each gray scale image has a resolution of

6 m/pixel [e.g., 25]. Our area of interest has been repeatedly covered by CTX observations from multiple viewing angles. We use a CTX stereo-pair (N05\_064204\_1384\_XI\_41S258W and K06\_055540\_1384\_XN\_41S258W) to derive high-resolution topography and orthorectified imagery of the study area, centered on  $-41.66^{\circ}\text{S}$ ,  $101.38^{\circ}\text{E}$ . We follow the established workflow [e.g., 43] to produce a Digital Terrain Model (DTM) with an elevation post-spacing of 18 m. First, we pre-process the images with the open source USGS Integrated Software for Imagers and Spectrometers (ISIS). Then we generate the DTM and the orthorectified images using commercial BAE Systems SOCET SET<sup>®</sup> photogrammetric software. We estimate the vertical precision of the DTM as a function of pixel scale and the convergence angle between the images, as indicated in the ISIS3 USGS guide [43]. Images N05\_064204\_1384\_XI\_41S258W and K06\_055540\_1384\_XN\_41S258W have a resolution of  $res_1 = 5.16$  m and  $res_2 = 5.06$  m respectively, and a stereo convergence angle of  $\theta = 10.51^{\circ}$ . Taking  $Corr = 1/5$  as an estimate of the precision to which position may be measured in an image (fractions of a pixel), the vertical precision of our DTM is given by [e.g., 44, 45]:

$$\frac{res_1 Corr}{\tan(\theta)} = 5.5 \text{ m.} \quad (1)$$

We use the CTX DTM to characterize LDA surface topography beyond the resolution of MOLA. The orthorectified images provide context for CaSSIS, and allow us to characterize reflectance variation where CaSSIS data is not available.

### 3. Key results and observations

#### 110 3.1. Topography and imagery

Reull Vallis has two segments: Upper and Lower Reull [33]. Our LDA of interest is located in Lower Reull,  $\sim 150$  km downstream from the junction of Teviot Vallis (figure 1, marked T). Reull Vallis displays here a boxy, trapezoidal cross-section (figure 2, inset) that is  $\sim 30$  km wide,  $\sim 1,500$  m deep, and with  
 115 a nearly flat floor measuring  $\sim 12$  km in width. The north-facing wall slope

is  $\sim 0.11$  and the south-facing slope  $\sim 0.10$ , with the north plateau averaging 100–200 m above the southern one.

Figure 2 shows the planform morphology (bottom) and topography (top) of this LDA. Guided by morphology, we structure our characterization of this deposit by dividing it into 8 regions, shown in figure 2: (1) area encompassing the horizontally banded material that makes the vallis wall above the LDA; (2) area characterized by the LDA structured in regularly spaced lobes that display arcuate bands with apex pointing down-slope, and that terminate in a front correlated with a topographic step: this marks the first terrace (hereafter, we name these terminations 'terraces'); (3) first to second terrace, where the LDA continues to be structured in similar lobes displaying also a well-defined termination; (4) second to third terrace, marking the end of north deposit in an inner trough; (5) inner trough, a linear feature running parallel to the direction of Reull Vallis that is offset from the Vallis center line; (6) southern deposit, composed of an LDA structured in lobes with long-axes pointing northwards, and terminating southwards of the inner trough; (7) smooth mantling material, with subdued lobate structures showing apparent continuity with those of the northern deposit; (8) southern rim.

### 3.1.1. Reflectance patterns

We use CaSSIS image cube MY34\_005511.224 in PAN, BLU (figure 3), CBRC (figure 6 and 4), and CTX K06\_055540.1384\_XN\_41S258W to study the deposit morphology. Regions 1-4 show high BLU reflectance values in CaSSIS (figure 3), with reflectance decreasing in the last terrace (4) towards the inner trough (5) and increasing again with the start of the southern deposit (6), smooth deposit (7), and towards the southern rim.

Lobe morphology, texture, and reflectance show variations across regions (1)-(7). Region (1) displays a material contrast, transitioning from a lower reflectivity in the BLU and PAN bands characterizing the layered, resistant material making the vallis walls, to a high reflectivity correlated with the smooth material that makes the LDA. The ridge-and-valley texture that makes the wall

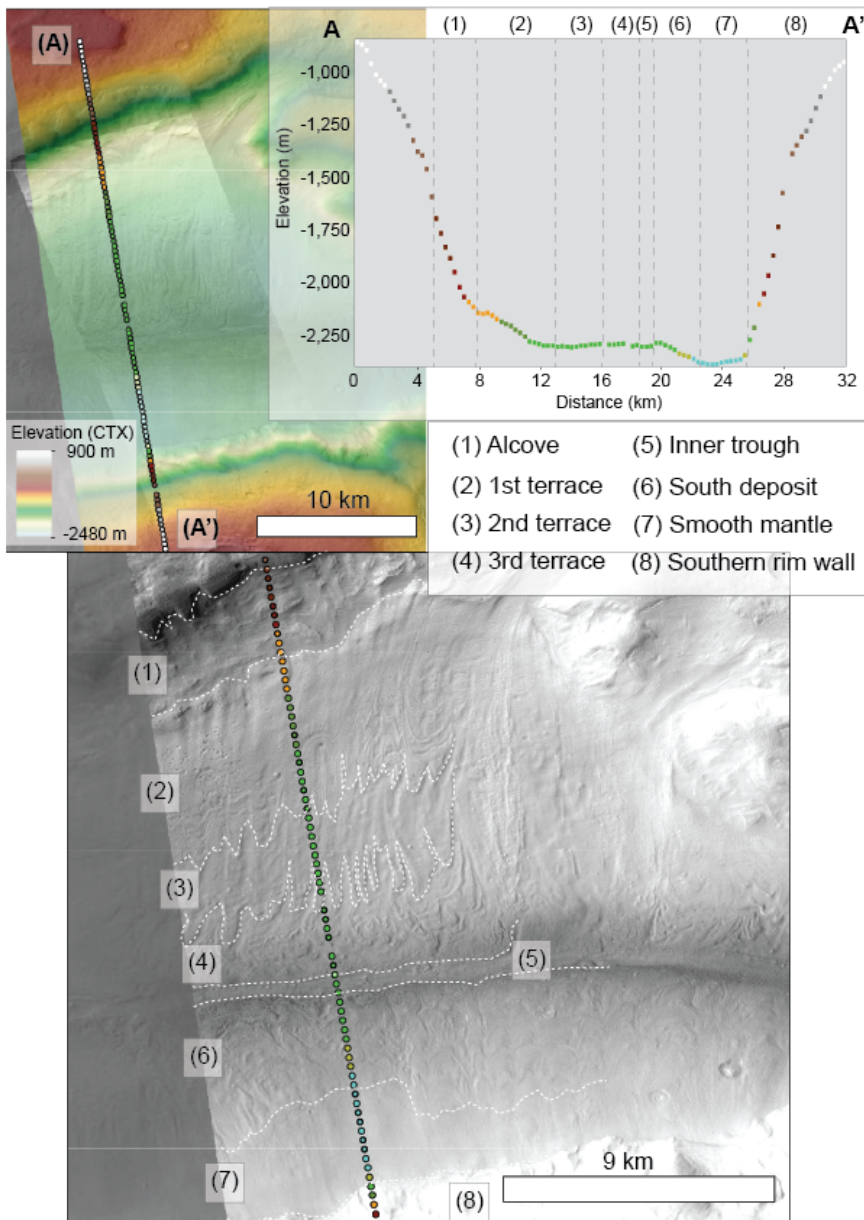


Figure 2: Topography and morphology of the LDA. Top panel: Topography (CTX, CaSSIS) indicating the MOLA altimetry track defining our A-A' cross section. Right: Cross-section (elevation vs. distance along A-A') showing individual MOLA laser shots color coded by elevation, annotated with the parts of the LDA (1–8). Bottom: Contrast-enhanced CTX image K06\_055540\_1384\_XN\_41S258W\_5m\_o showing the boundaries between morphological zones 1–8 (white dashed lines).

topography in region (1) (figure 2) continues as linear troughs in region (2), with lateral changes in reflectivity mapping these patterns. To the west, the texture is pitted with knobs puncturing the deposit.

In region (3) regularly-spaced lobes develop with a well-defined interior arcuate banding pattern (figure 3), which is discussed in more detail below. Reflectance in the PAN and particularly the BLU bands highlights the banding pattern in the downslope and across-flow directions.

The inner trough (5) displays the lowest reflectance in the image as well as the lowest albedo, with minimum values correlated with both sides and decreasing to the east of the image.

In the south deposit (6), CaSSIS BLU reflectance still shows a banding pattern (each band is  $\sim 35$  m wide) that fades gradually onto region (7). Unlike the north deposit, there is no visible terminal flow fronts nor a strong reflectance contrast marking the existence of terraces. Instead, the texture continuously changes from subdued lobes to a much smoother surface with a higher reflectance, showing small pits possibly signaling ice ablation processes, as described in next section.

### 3.1.2. Morphology of surface structures

We analyze the surface LDA morphology from small scale to full cross-section scale as shown in figure 4.

**Arcuate bands** CaSSIS and CTX data show fine-scale arcuate banding patterns alternating between high and low reflectivity, convex in the down-flow direction (arrows in figure 4a). Arcuate bands widen along the deformation axis and narrow in cross-slope, with individual band measuring  $\sim 30$  m in the cross-slope direction. Alternating reflectance patterns in the composite CBRC image may suggest either a surface or compositional difference. An example of the first would be the accumulation of materials of a particular grain size, and an example of the second, a difference in composition (e.g., an ice-rich matrix and substrate). The resolution of the CTX DEM did not allow us to assess whether arcuate bands display crest-and-valley topography associated with the

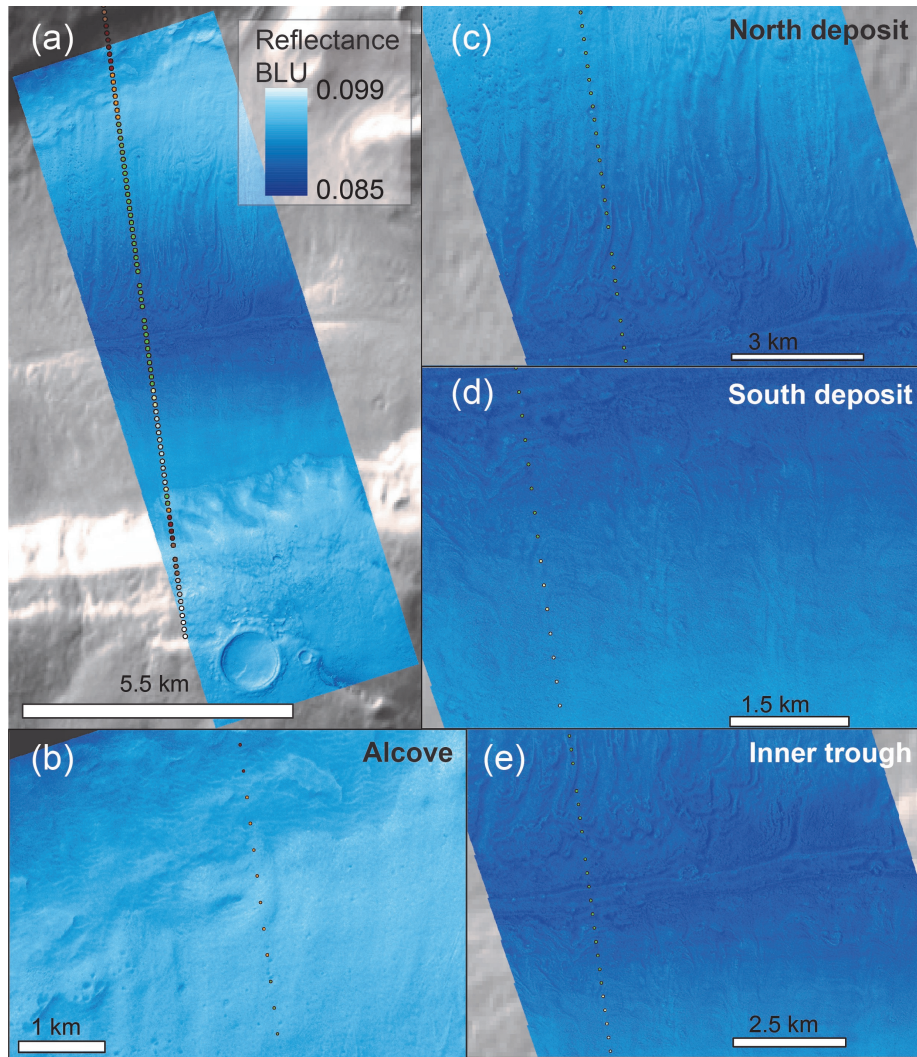


Figure 3: THEMIS daytime IR data (NASA/ ASU) overlapped with CaSSIS BLU color band (ESA/ Roscosmos/ CaSSIS) stretched at 2.5 standard deviation for panels (a)-(e). (a) Overview of CaSSIS MY34\_005511.224 and footprint extent. (b) Deposit alcove (zone 1). (c) North deposit (zones 2-4). (d) south deposit (zones 6-7). (e) inner trough (zone 5).

reflectance banding pattern.

**Periodic lobes.** Sets of lobate structures that are elongated in the down-flow direction are found spaced regularly in the cross-flow direction in both north and south deposits (see figure 4b). Lobes are particularly prominent in the north deposit, particularly in zones 2, 3, and 4. Lobes emerge in zone 2, where they display larger widths that narrow towards zone 3. At the elevation of zone 4, lobe regular spacing tends to widen, with a gradual dissipation of the spacing pattern towards the inner trough. Nested within each lobe, both arcuate bands and ridge-and-valley textures are visible, with the first dominating in flow fronts of zone 2, and the latter more common in zones 3 and 4. The resulting pattern in the down-flow direction is of 3 distinct terraces, visible in the topographic data. As opposed to arcuate bands, lobes are both reflective and topographic features, as resolved by CaSSIS, CTX, and the CTX DEM.

**Fine-scale textures** Lobe surfaces display a ridge-and-valley longitudinal texture, found also in other LDAs in this region [30]. This texture is characterized by a succession of ridges and troughs that are of the same scale as arcuate bands, but that are linear and oriented oblique to the main direction of deformation, as visible in figure 4c. Pitted textures with presence of knobs also appear, predominantly in the lower flow fronts (figure 4d). We interpret this texture to be the product of thermokarst sublimation of ice, following previous work [49, 50].

**Terraces.** Lobe terminations are distributed in terraces visible both in image and topography, as shown in figures 4e and 5a. Inter-lobe spacing in terraces measured in the cross-slope direction varies among regions, with region 4 displaying larger spacing than fronts in regions 2 and 3.

### 3.2. Analysis of dominant length scales

In this LDA we also identify three scales of repeating patterns which are probably deformational and/or structural in origin, as shown in figure 5: The distance between terraces ( $\Delta L$ ), the spacing between lobes ( $\lambda$ ), and the width of arcuate bands ( $\gamma$ ). All three features are clearly visible using CTX and CaSSIS

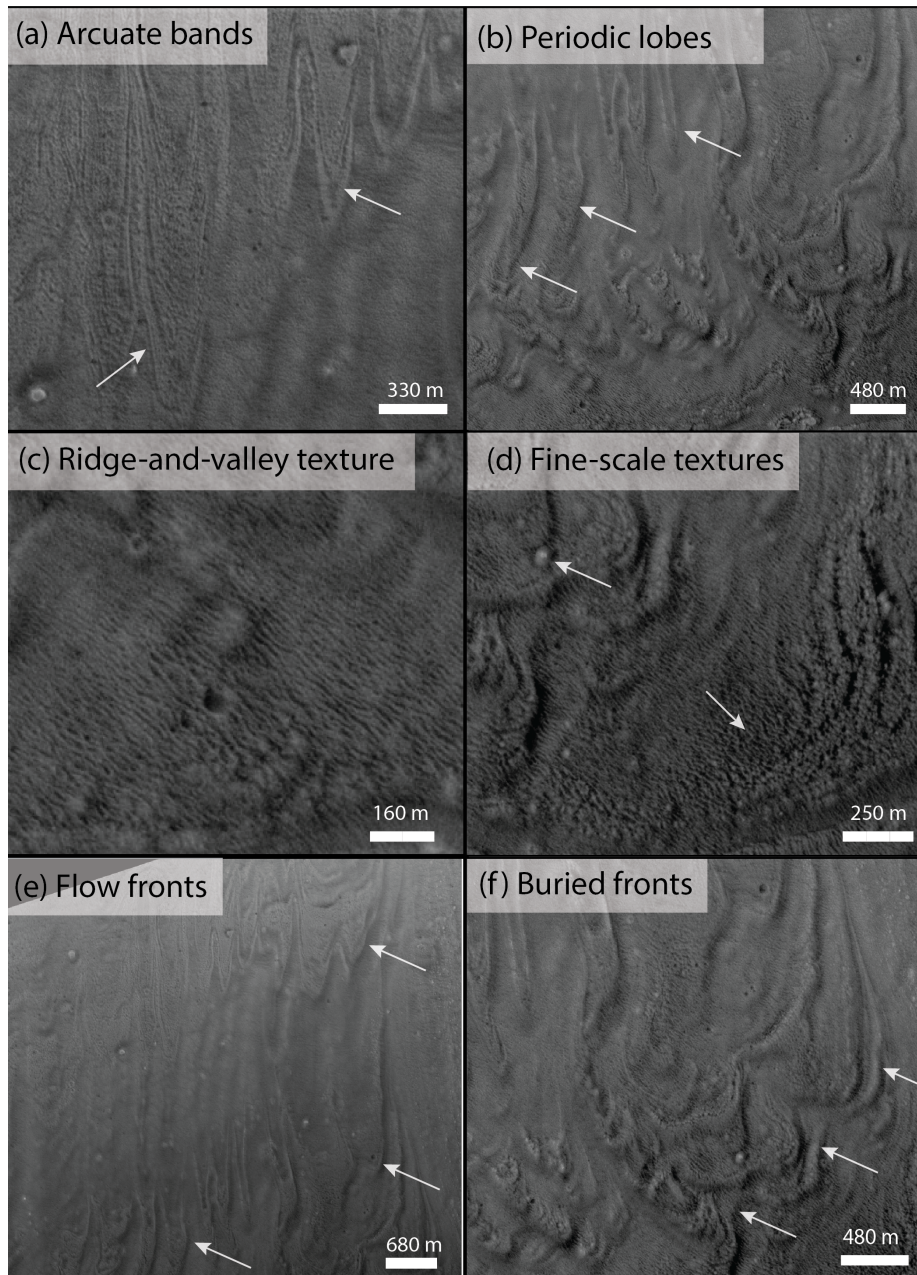


Figure 4: CaSSIS PAN colour band showing the morphology of the area of interest. (a) Arcuate banding patterns showing convex nested bands alternating in reflectance. (b) Periodic lobes elongated in the down-flow direction, showing regular spacing. (c) Ridge-and-valley texture. (d) Knob (left arrow) and pitted texture (right arrow) found predominantly in the lower flow fronts on the north deposit. (e) Flow fronts marking the topographic terracing associated with lobe terminations. (f) Buried fronts showing possible compressional deformation.

data, and the first two are within the resolution of the CTX DEM.

We now focus on characterizing these patterns under the assumption that they can be related to the deformation of ice or icy material within the LDA [e.g., 51], and with a focus on the northern deposit (zones 2-4). We seek to  
210 quantify the dominant wavelengths that characterize the lobe spacing, as well as the length scales of each individual band, comparing results obtained using image and topographic data from CTX. To optimize data return from CaSSIS reflectance, we first increase the contrast in the banding structure, so that relevant intensity vs. distance spatial series can be produced.

215 We find that with a color composite image obtained using a ratio of (1BLU-4PAN)/(4PAN/BLU) bands ([22], substituting NIR with PAN), we are able to highlight the inter-lobe space, as well as the arcuate banding pattern (figure 6). We then use a spectral density estimation to identify the dominant wavelengths in the transverse directions ( $\lambda$  and  $\gamma$ ) as defined in figure 5, which will drive  
220 our discussion. We use the CBRC product to acquire a set of profiles across the lobes mapping intensity with respect to distance (figure 6 and supplement).

Each transverse profile t1-t10 is obtained perpendicular to the flow direction (note how the transect lines are not parallel) at successively lower elevation, whereas we use longitudinal profiles (l0-l10) aligned with the deformation axis  
225 to interrogate arcuate band widths. Transverse profile t1 and longitudinal profile l0 correspond to the spatial characteristics of the basal unit, visible before the detachment of the icy deposit in region 1 (e.g., figure 3, bottom left, and 6, l0 and t1). Note that the CaSSIS image footprint does not extend to cover all transects and lines of interest (figure 6). Where the lines t1-t10 or l0-l10 extended beyond  
230 the image, we used CTX K06.055540\_1384\_XN\_41S258W\_5m.o.

Spectral analysis requires prior detrending and demeaning of the data. Factors such as terrain roughness, noise, presence of clouds, etc. may affect the image reflectance and introduce random noise at smaller wavelengths. To address these we use an order 4 Butterworth filter, that is, a band-pass filtering  
235 function with a stopband defined by twice the Nyquist frequency (given by the resolution of CaSSIS, 4.6 m/pixel) combined with the python “filtfilt” function

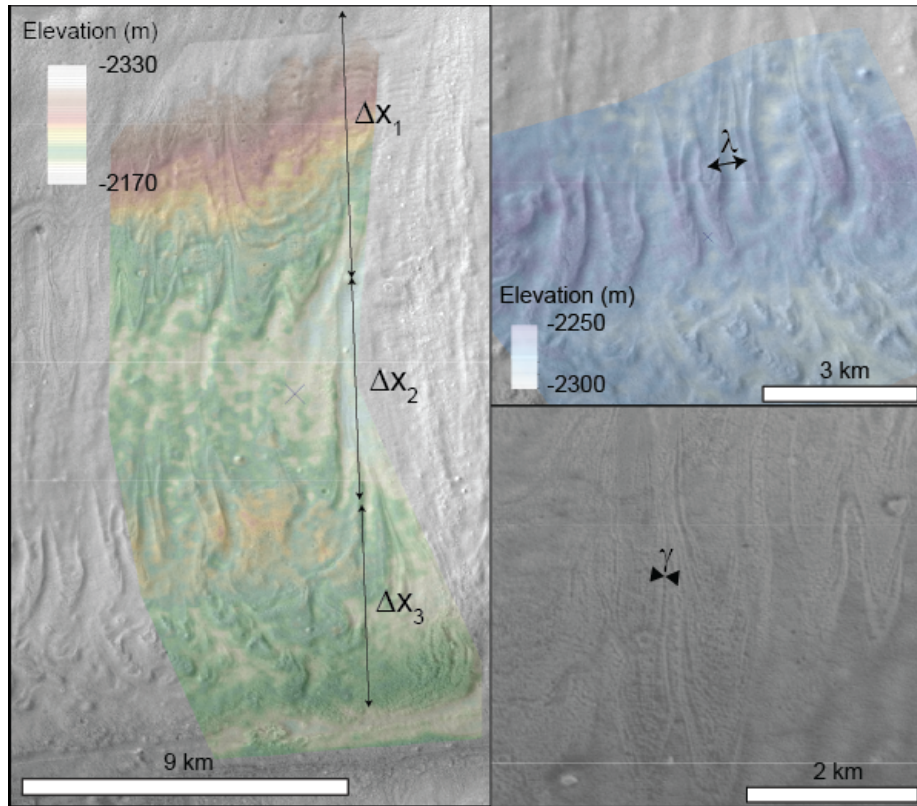


Figure 5: Characteristic spatial scales of the LDA. Left: CTX K06.055540\_1384\_XN\_41S258W\_5m.o overlapped by CTX DEM showing the inter-terrace distance  $\Delta x_1$ ,  $\Delta x_2$ ,  $\Delta x_3$ . Terrace termination is defined by a step in topography (overlying image data) as well as with a marked lobate flow front. Right (top): CTX K06.055540\_1384\_XN\_41S258W\_5m.o overlapped with CTX DEM showing the wavelength  $\lambda$ , marking the regular spacing between deforming lobes. Right (bottom): CaSSIS image MY34.005511.224 showing reflectance variability between arcuate bands, alternating at a distance  $\gamma$ .

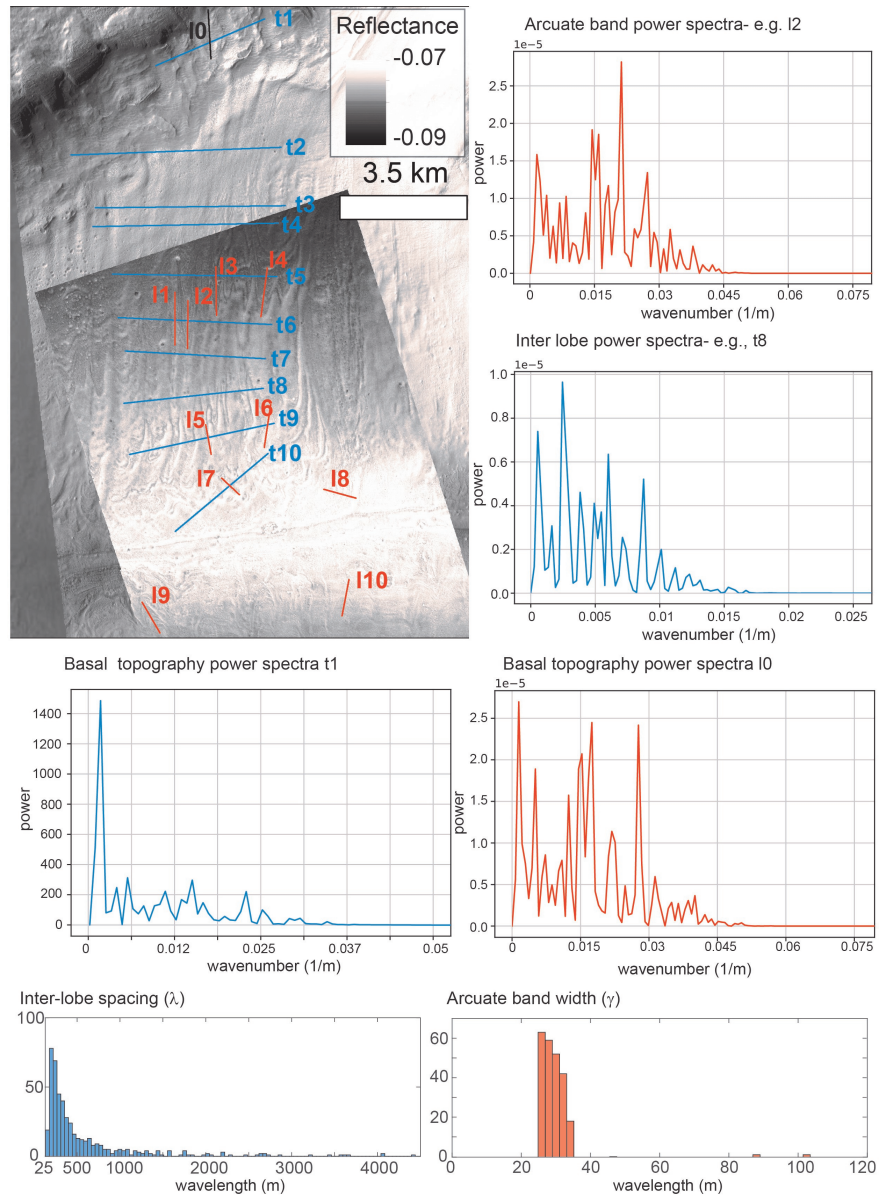


Figure 6: (a) CaSSIS CBRC overlaying CTX K06.055540.1384.XN.41S258W.5m.o, with transverse profiles (t1-t10) in blue, and longitudinal profiles (l0-l10) in orange. (b,c) example power spectra for arcuate bands (b) and for lobe spacing (c). (d,e) Power spectra corresponding to the spatial characteristics of the basal deposit ((d),transect t1, (e) long section l0). (f,g) histogram showing counts vs. wavelength for all transect profiles t2–10 (left), with peak corresponding to most common  $\lambda$ , and all longitudinal profiles l1–l10 (right) with peak corresponding to most common  $\gamma$ .

(scipy, signal toolbox), a zero-phase forward and reverse digital IIR filtering function with polynomial coefficients weighted by the length of the spatial series. After pre-processing, we perform a fast Fourier transform algorithm (fft) on the spatial data series. Examples of the resulting power spectra are displayed in figure 6 and the supplement.

Predominant wavelengths in CBRC intensity (figure 6) have higher power values, whereas less common wavelengths score smaller powers. Acquiring the spatial series data in ArcGIS, with transects representing reflectance intensity vs. distance, we explore which wavelengths  $\gamma$  and  $\lambda$  peak commonly, and are thus predominant. We quantify the frequency of each wavelength (in smaller arcuate bands  $\gamma$  and larger lobes  $\lambda$ ) using histograms (figure 6), with orange color for arcuate bands and blue for lobes.

The distance between terraces  $\Delta x$  is measured directly from image data from region 1 to the deformational flow front in region 2 ( $\Delta x_1$ ), and from front to front in zones 3 and 4 ( $\Delta x_2$  and  $\Delta x_3$ ) as shown in figure 5.

### 3.2.1. Summary of results

We find  $\lambda \sim 180 - 350$  and  $\gamma \sim 25 - 33$  m to best describe inter-lobe spacing length and arcuate band width, respectively. Inter-terrace distance, as defined in figure 5, is found to be  $\Delta x_1 = 5800$  m with  $\sigma_1 = 400$  m;  $\Delta x_2 = 3100$  m with  $\sigma_2 = 400$  m, and  $\Delta x_3 = 2300$  m with  $\sigma_3 = 400$  m. Whereas the direction of maximum deformation is linear in terraces 1 and 2, the deformation axis is significantly curved in terrace 3, suggesting a complex strain history in response to a combination of stresses.

### 3.3. SHARAD observations

We analyzed six SHARAD observations that overlap our region of interest (product ID: S\_00365901, S\_00878801, S\_01301401, S\_01700301, S\_03948601, S\_05716901), available in the Planetary Data System (PDS). In order to accurately interpret the SHARAD radargrams and characterize the subsurface, it is essential to differentiate clutter from real subsurface reflections [40]. In partic-

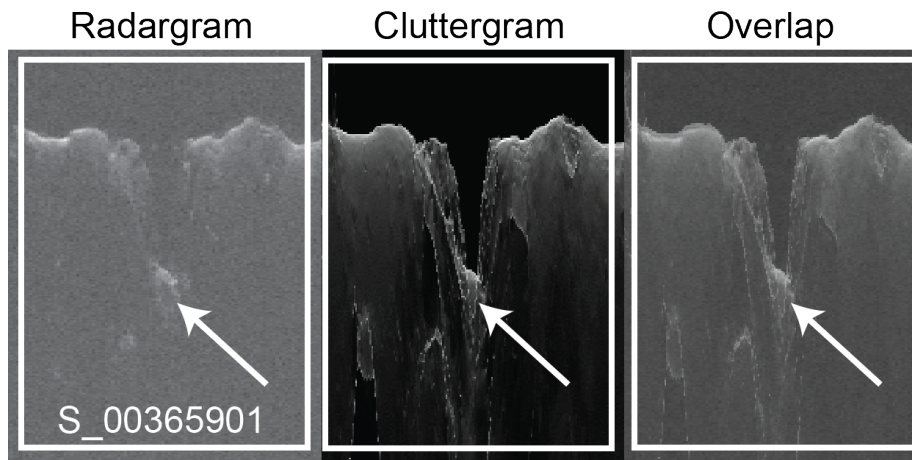


Figure 7: SHARAD observation S\_00365901 over the area of interest. (Left) Radargram, note the presence of a possible subsurface reflector (arrow). (Middle) MOLA clutter simulation. Note the presence of clutter where the reflector is (arrow). (Right) Image showing an overlap of the radar and cluttergram to highlight the presence of multiple clutter reflectors correlated with the position of the possible reflector.

ular, false subsurface returns are a concern given the steep walls of Reull Vallis (see e.g., figure 2).

Using the QDA processor via the CO-SHARPS processing boutique [52], we produced MOLA clutter simulations (“cluttergrams”) corresponding to these six SHARAD observations. We present the results from analyzing S\_00365901 in figure 7. Reflected signals from the walls of Reull Vallis (sections 1 and 2) are not recorded in the radargram. This could be caused by two factors: (1) Steep topography may sometimes reflect radar signals away from the receiver resulting in signal being lost, and (2) Synthetic aperture processing of radar data can sometimes attenuate reflected signals from interfaces that slope along-track.

The radargram (figure 7, left) shows a subsurface reflection at the bottom of Reull Vallis (arrow), which could indicate the presence of buried ice (or high-density bedrock) correlated with sections (3) and (4). However, when the radargrams are compared against cluttergrams, these reflectors cannot be distinguished from surface clutter (figure 7 center and right, also supplement).

A similar result is found when analyzing the other five SHARAD observations (supplement).

### 3.4. Data integration

We analyzed the presence of ice in the surface with the CaSSIS BLU band and in the subsurface with SHARAD radar data. Whereas the CaSSIS BLU band shows that reflectance correlates with the lobe banding structure, we interpret this to be a result of surface roughness variability due to flow front accumulation patterns, and not indicative of the presence of surface ice. Radar data is inconclusive: It is difficult to assess whether ice is indeed present in the vallis and driving the instability on the flank and into the valley bottom, or the reflections observed are solely the result of clutter. Lack of clear subsurface reflectors can also be due to a homogeneous mixture of debris and ice in the subsurface, making a clear dielectric contrast surface nonexistent.

Image data provides the most solid argument for the presence of buried ice in this deposit through the evidence for deformation in the surface morphology, and the overall consistent surface morphology and spatial assemblage of landforms as seen in other VFF that are known to contain ice. The three length scales analyzed in this section (inter-terrace distance, inter-lobe spacing, and width of arcuate bands), in particular, are useful indicators of the type, direction, and magnitude of stresses, past deformation history, and relevance of boundary conditions. We dedicate the next section to discussing the interpretation of these length scales.

## 4. Discussion and interpretation

### 4.1. Characteristic lengthscales: hypotheses of formation

We aim to interrogate the emplacement and evolution history of this LDA from the three length scales measured in previous sections. To drive this discussion, we present and test hypotheses for the emplacement and evolution of these spatial characteristics, as well as their relationship with the environmental (boundary) conditions and stratigraphy. Our leading hypotheses are:

- 310 •  $H\lambda_1$ : The regular inter-lobe spacing is a result of the deformation of ice on top of regular bed topography, as suggested by the similarity in wavelengths (transect t1 in figure 6).
- $H\lambda_2$ : The regular spacing found among lobes is a result of a viscous fingering instability, similar to that occurring in gelifluction or solifluction lobes.
- 315 •  $H\Delta x_1$ : The existence of visually and topographically distinct terraces is a result of discrete pulses of enhanced glacial creep deformation.
- $H\Delta x_2$ : The existence of visually and topographically distinct terraces reflect steps in the basal topography underneath the icy deposit.
- 320 •  $H\gamma_1$ : Arcuate bands reflect changes in accumulation/ablation patterns, similar to band ogives [53, 51, 6], arcuate surface discontinuities [54], or boulder bands on Mars [55].
- $H\gamma_2$ : Fine-scale banding is a form of arcuate foliation patterns as seen in terrestrial glaciers [56, 57, 51, 6]. Banding here reflects the cumulative deformation patterns experienced by the ice, including its internal stratigraphy [58, 6].
- 325

4.1.1.  $H\lambda_1$ : *Do lobes preserve the bed topography spacing found in the source region?*

The topographic variability found in region 1, and its similar scale compared to inter-lobe spacing (see transect t1 in figure 6) suggests that this pattern may have propagated down-slope with ice flow. To interrogate whether the presence of lobes in this deposit can derive from variations in ice thickness due to the basal topography in region 1, we consider a model where a layer of ice covers uniformly a substrate with presence of regularly spaced 'bumps' in the cross-flow direction. At the base of this ice layer, the pressure of the ice is given by its bulk thickness ( $h_o$ ) plus/minus small variations given by the substrate topography, with amplitude  $A_y$ . As a consequence of these small variations,

330

335

small harmonic stresses develop in the cross-flow direction. Because ice is a strongly non-Newtonian flow, and deformation in any given direction depends  
 340 on total stresses, deformation in the  $x$  direction (downflow) with variations in the  $y$  direction (cross-flow) may exist, leading to the development of periodically spaced lobes through time.

To test this hypothesis, we perform a stability analysis of a layer of ice deforming down a slope. Here, bulk (or mean) ice thickness is taken to be  
 345 enough to drive deformation (stress in excess of yield stress), and variability in this parameter is given by the cross-flow topography of region 1, and is small in comparison:  $A_y/h_o \ll 1$ . We let  $x$  be the direction of ice surface slope (downflow direction),  $z$  be the vertical direction, perpendicular to ice surface, and  $y$  the cross-flow direction. Assuming this initial setup, ice thickness is given by:

$$h(y) = h_o \left[ 1 + \epsilon \sin \left( \frac{2\pi y}{\lambda} \right) \right] \quad (2)$$

350

The resulting stresses are:  $\sigma_{xz}$  typical of ice masses resting on a slope, and given by the bulk ice thickness and surface ice slope in the  $x$  (down-flow) direction; and the much smaller  $\sigma_{yy}$ ,  $\sigma_{zz}$  and  $\sigma_{yz}$  resulting from the cross-flow gradients in ice thickness. These stresses constitute the stress tensor, from which the deviatoric tensor  $\tau$  is calculated to derive deformation directions and rates:

$$\tau = \sigma - \delta\sigma_M, \quad (3)$$

where  $\sigma_M = 1/3(\sigma_{xx} + \sigma_{yy} + \sigma_{zz})$  and  $\delta$  is the kronecker delta. The next step is to relate the stress field experienced by this icy deposit to the final deformation structures, to analyze the possible formation of regularly spaced lobes. Total deformation rates, including directions and magnitudes, are given by the rate of strain tensor  $\dot{\epsilon}$ , which is related to the deviatoric stresses through the Nye-Glen law [6]. We are interested in the variations in ice deformation experienced in the cross-flow ( $y$ ) direction as the ice flows downstream ( $x$ ) driven by its own

weight ( $z$ ). That is, we want to know  $\dot{\epsilon}_{xz}(y)$ , which is given by:

$$\dot{\epsilon}_{xz}(y) = A(T)\tau_E(y)^{n-1}\tau_{xz}(y), \quad (4)$$

where  $\tau_E$  is the effective stress (second invariant of the deviatoric stress tensor). We derive a first order approximation to this strain rate using linear stability analysis (see the supplement for more derivation details). Our result shows that the rate of deformation in the downslope direction ( $\dot{\epsilon}_{xz}$ ) becomes a harmonic function of the cross-flow direction ( $y$ ), with the same wavelength content of the topography in region 1:

$$\dot{\epsilon}_{xz} = A(T)(\rho g)^3(h_o - z)^2 \sin(\theta)^3 \left[ (h_o - z) + 3\epsilon h_o \sin\left(\frac{2\pi y}{\lambda}\right) \right] \quad (5)$$

The basal topography existing in region 1 therefore can trigger the development of regularly spaced lobes with the same periodic characteristics, influencing the planform morphology of the deposit (see supplementary information for a model illustration). After a long period of time, the ice columns that were  
 355 originally thicker in region 1 (where the total thickness is  $h_o + A_y$ ) will have flowed more than the originally thinner sections ( $h_o - A_y$ ) and will develop lobes, with a length influenced by temperature (through ice softness  $A(T)$ ) and bulk ice deposit thickness ( $h_o$ ). Total deformation is given by the time integral of equation 5. For this process to be possible, the bulk thickness of the ice deposit  
 360 needs be of at least  $h_o \sim 150$  m, setting the driving stresses equal to the yield strength of ice (taking the yield stress  $\tau_o = 50 - 100$  kPa).

#### 4.1.2. $H\lambda_2$ : Do lobes reflect gelifluction processes?

Gelifluction is the downward movement of topsoil due to freeze-thaw processes, in particular segregation ice growth and frost heave [59]. Landforms  
 365 associated with gelifluction are organized in terraces in the downslope direction, and in regularly spaced lobes in the cross-flow direction [59, 60], with a morphology that visually resembles that of the LDA under study. It is typically observed on Earth in periglacial landscapes [59], with similar landscapes observed on Mars [61]. Ice in gelifluction lobes is distributed within the pore  
 370 space, without vertical organization [59, 60].

A recent study [62] proposes a physical explanation (equation 6) for the down slope movement of Arctic topsoil, with applications to proposed martian gelifluction lobes that is consistent with analogue observations [63, 64, 65, 66]. This model explains how regularly spaced lobes arise as the result of the competition between body forces (gravity), cohesion forces at the flow front, and lateral flow due to hydrostatic pressure under topographic bumps. Scaling development of the flow dynamics equations, and stability analysis derives a regular wavelength described in terms of [62]:

$$\lambda = C \sqrt{\frac{h_c \beta}{2S}} \quad (6)$$

Where  $h_c$  is a characteristic thickness,  $\beta$  is the horizontal scale describing variations in viscosity, and  $S$  is the ground slope.  $C$  is an empirical constant (field data supports  $C=6$ ), validated for Earth. We acknowledge that the lack of measurements specific to Mars may introduce error in the estimation of  $\lambda$  through this method. Improved understanding of the characteristics of the substrate on Mars will help improve this calculation. Cross-slope wavelength therefore increases with thickness and cohesion forces and decreases with steeper slopes.

We contrast the results for  $\lambda$  in the previous section with predictions from this equation, taking  $C=6$ ,  $h_c=5$  m (order of magnitude), and slopes of  $S \sim 0.1$  and  $S \sim 0.01$  to capture the present day slope as well as a possible paleoslope (based on the cross-section of Reull Vallis just upstream from this site). We then assume that variations in viscosity  $\beta$  are given by the presence of dust, soil, melt fraction, and rocks (supplement). The internal debris content of LDA and LVF is constrained to be  $<10\%$  based on radar observations [14]. Detailed studies of LDAs within Deuteronilus Mensae [67] indicate that 20% of the surface has high boulder abundance in this region, with higher concentrations found near the terminal fronts. We adopt both of these numbers assuming that they are representative of this LDA, although we acknowledge the need for a detailed analysis using HiRISE and TES/ THEMIS data that is out of the scope of this paper. Based on these measurements, we choose  $\beta \sim 1.5$  m (supplement) and

we derive an expected wavelength of  $\lambda \sim 115$  m (taking  $S=0.01$ ) and  $\lambda \sim 35$  m taking  $S=0.1$ , using equation 6. The lengthscale observed in the LDA is a factor four larger than that predicted by equation 6.

395 The results obtained are consistent with the lobe spacing  $\lambda$  measured in section 3.3 within order of magnitude, which does not allow us to definitely reject this hypothesis. However, gelifluction requires the presence of a certain degree of liquid water in the deposit to allow for soil creep, which is hard to justify in the near-surface of Amazonian Mars. Therefore, we favor the previous  
400 hypothesis ( $H\lambda_1$ ) to explain the formation of regularly-spaced lobes given the consistency between the spatial scales of region 1 and inter-lobe spacing. This interpretation requires the deposit to be thin, be subject to small stresses, and therefore to deform very slowly.

#### 4.1.3. $H\Delta x_1$ : Do terraces reflect discrete episodes of deformation?

405 Terraces are associated with the termination of lobe apices, and are visibly associated both with deformation of the deposit and a topographic signature. Our observations of this LDA show no fracture patterns, including crevasses, meaning that the tensile stresses this deposit experienced were always below those of ice fracture, and therefore that strain rates were exceedingly slow. In  
410 the current surface temperature conditions, surface or near-surface ice flow is below detection rates on Mars, consistent with observations for low strain rates in this LDA and expectations from models of ice flow elsewhere on Mars [e.g., 68, 69].

However, deformation did occur in this deposit judging from the morpholog-  
415 ical patterns, and several aspects could have facilitated ice deformation in the past. The most important parameter controlling ice creep would be temperature [6]. Warm spells occurring during or after the time of deposit emplacement would have exponentially decreased ice viscosity, making ice softer and helping mobilize layers of icy material downslope. The second player are total  
420 stresses, which have a quadratic influence in ice effective viscosity. Increased total stresses, including driving stresses and pressure, would have facilitated ice

flow. This includes steeper ice surface slopes, layers of englacial denser material or presence of a thick debris cover (increasing density), and a thicker ice deposit.

Stresses, however, remained always below the critical stress for brittle fracture in this deposit, because crevasses and other fractures are not observed at  
425 this resolution. Given the slow nature of ice flow in cold temperatures and the low strain rates inferred and observed, and based on the current understanding of ice rheology, we consider that past warmer episodes are likely necessary to explain the deformation fronts. Topographic signatures associated with terraces can then be explained by accumulations of ice and debris where the flow  
430 stopped moving, because of lower temperatures, lower driving stresses (i.e., thinner flows), or a combination. We also note also that englacial entrained debris can have an important effect on ice viscosity, leading to both weakening and stiffening behaviors depending on its concentration and stratigraphy [70, 71].  
435 Without a deeper understanding of the dynamics of ice-debris mixtures [70], it is hard to quantify exactly the effect of debris in the rheology of this deposit.

Distinct warmer spells, driven, e.g., by obliquity variations, could have contributed to the formation of several episodes of deformation, producing distinct flow fronts. The presence of the several terraced fronts of deformation would be  
440 hardly consistent with a single episode of warming (and/or high stress regimes driven by enhanced accumulation), and would require distinct episodes of glacial advance. This remark is consistent with previous studies of boulder accumulation bands in debris covered glaciers [55].

#### 4.1.4. $H\Delta x_2$ : Do terraces reflect steps in the basal topography?

Whereas the thickness of the deposit could not be estimated quantitatively  
445 from radar data, thinning of the deposit due to ice sublimation likely occurred since the episodes of deformation recorded in the surface morphology. This is supported by the presence of pitted textures (figure 4d), and the mismatch between current topography and deformation directions. An association of terraces with basal topographic steps is further supported by the correlation of arcuate  
450 bands with the topographic steps associated with terraces. Both ogives and

foliation patterns, invoked to explain the presence of these bands (hypotheses  $H\gamma_1$  and  $H\gamma_2$ ) tend to form associated with areas of intense deformation such as steep slopes [e.g., 53, 72, 51, 6]. Additionally, ice deposits tend to smooth  
455 subglacial topography so that surface wavelengths grow with ice thickness and ice viscosity [e.g., 73].

Given the correlation of arcuate bands with topographic steps, we consider that basal topography played a role in defining terraces. We therefore invoke a synthesis of hypotheses  $H\Delta x_1$  and  $H\Delta x_2$  to explain terraces, given the spatial  
460 association of deformation fronts, arcuate bands, and surface topography. Indeed, the presence of basal topographic obstacles could have provided a natural barrier for a flow deforming slowly, at low driving stresses, and under largely cold temperatures. This flow could then accumulate, so that the visible topographic signature is a combination of basal topography and thickened parts of  
465 the deposit, with the later likely a bigger contribution than the former.

#### 4.1.5. $H\gamma_1$ : Are the arcuate bands related to mass balance cyclicity?

Ogival bands are arcuate bands that extend across the surface of terrestrial glaciers, with albedo patterns alternating between dark and light and convex in the direction of flow [e.g., 53, 51]. When associated with ice falls, ogives  
470 result from a combination of variations in ice deformation and mass balance [e.g., 53, 72, 6, 74].

ASD (arcuate surface discontinuities) are another type of mass-balance driven banding (hereafter referred to as MBDB). ASD form as follows [54]: (1) During obliquity-driven ice accumulation periods, exposed ice is found at the accumu-  
475 lation zone and becomes covered by a debris layer that thickens down-slope. (2) When conditions shift to net ablation, ice loss occurs predominantly where ice was exposed at the surface, with reduced rates of sublimation where ice is buried under thicker debris lags. Eventually a spoon-shaped depression forms near the original accumulation zone where a lag of debris develops, involving  
480 the exposure of englacial debris, rockfalls from the alcove, and dust. (3) When conditions shift again to net accumulation, snow and glacial ice infill the spoon-

shaped depression, and glacial creep deforms and transports the filled depression downflow, forming a raised arcuate band. Upon multiple successions, arcuate bands displaying alternating patterns of surface debris roughness develop.

485 CaSSIS data helps to distinguish band ogives from ASD. The difference in reflectance between bands in the composite CaSSIS CBRC image may suggest either a surface or compositional difference, as pointed out in section 3.1.2. Given the lack of surface ice exposure observed with CaSSIS PAN, BLU, and CBRS bands, we favor the former. The arcuate banding observed is then more  
490 consistent with ASDs identified on cold-based glaciers in Antarctica [54] and boulder banding patterns on a small set of LDAs on Mars [55]. An ASD origin hypothesis would predict spoon-shaped depressions to appear in the current interglaciation conditions, and these are indeed visible in the CTX topography inside lobe terminations (see figure 5b). MBDB are furthermore directly  
495 attributed to long-term environmental variations on Earth and Mars [54, 55], reflecting changes in accumulation and ablation tied with ice deformation.

If these bands are MBDB, mass-balance variability would likely be related to obliquity cycles as opposed to yearly cycles, in agreement with previous work [55]. In this case,  $\gamma$  corresponds to the distance ice deformed between periods  
500 of low and high accumulation, placing constraints on ice viscosity, deformation rates, and local temperatures [6]. As discussed before, the strain rates of this deposit were exceedingly low through history, so that variations across long periods of time of accumulation, flow, and ablation, would be required for ice to produce these patterns.

#### 505 4.1.6. $H\gamma_2$ : Are the arcuate bands foliation patterns?

Foliation is a planar or layered structure that develops in a glacier during flow, and that produces the compression, folding, and deformation of any heterogeneity within the ice. Terrestrial foliation structures are laterally continuous for no more than a few meters, and typically 10 to 100 mm thick [e.g., 51, 6].

510 To interrogate the presence of foliations leading to arcuate banding, we compare their characteristic wavelength to that of the layered deposit exposed in the

alcove region (1, figure 2), as well as with an exposure of layering within a similar deformable material exposed 14 km downslope Reull Valles. We use HiRISE image ESP\_049593.1390\_RED with center coordinates 100.78°E, -41.02°N for  
515 the purpose of measuring layer thickness, that captures an area north-west of our site and along the south facing slope of Reull Vallis (supplementary information, figure S4), bearing in mind that this image corresponds to a slightly different location. Each vertical layer in this exposure measures  $\sim 20$  m (after accounting for a surface slope of  $\sim 0.15$  and a planform distance of  $\sim 100$  m),  
520 comparable to the wavelength measured for the stratigraphy in the region 1  $\gamma_1 = 42 - 35$  (transect 10 in figure and corresponding power spectra 6). Power spectra using HiRISE data was not attempted owing to the high spatial resolution and consequent high frequency structure that would hinder a comparative wavelength analysis.

525 Terrestrial foliation patterns tend to be discontinuous [e.g., 51, 6], but at the resolution of CaSSIS and CTX it is not possible to evaluate the lateral continuity of arcuate bands. It could very well be the case that both foliation and mass-balance driven banding are present in this deposit. However, the strong spatial correlation of these arcuate bands with surface slopes (terraces) as well as their  
530 morphological similarity to terrestrial ASDs support the previous hypothesis more strongly.

We can assert, however, that both possible interpretations tie the arcuate pattern with time: boundaries between individual strata are likely isochrones [6, 75], and mass-balance driven banding patterns can be linked to the rate of ice  
535 deformation within an accumulation/ablation cycle [53, 6]. Following the analogue to terrestrial cold-based glaciers [54], we favor the hypothesis that arcuate bands in this deposit may reflect mass balance cyclicity driven by obliquity variations, tying original ice thickness, ice creep velocity, time between accumulation and ablation episodes, and temperature conditions into the surface morphology  
540 of martian LDAs.

Table 1: Deformation lengthscales and strain

Lobe	Region	$L1$	$L2$	$\varepsilon_{xy}$
Lobe 1	2	5550	1700	2.3
Lobe 2	2	3740	2600	0.4
Lobe 3	3	10960	6500	0.7
Lobe 4	3	11190	6700	0.7
Lobe 5	3	38460	6700	4.7
Lobe 6	3	33920	7600	3.5
Lobe 7	4	7930	7000	0.1
Lobe 8	5	5190	3100	0.7
Lobe 9	5	3918	2100	0.9

#### 4.2. Deformation history of this LDA

Mapping and quantifying the total deformation (finite transversal strain  $\varepsilon_{xy}$ ) is important to understand the history of this deposit: It is the time integral of all combined strain rates (i.e. equation 5). To quantify deformation we measure the relative difference between the deformed ( $L1$ ) and an initial length ( $L2$ ),  
545 divided by  $L2$ , using the CaSSIS CRBC image. We define  $L1$  as the length along selected arcuate bands, and we take  $L2$  as transverse to flow direction expanding the extent of the banded lobe in a straight line. To evaluate these parameters, we mapped the lines along continuous ogival bands using ArcGIS (supplement),  
550 and calculated  $\varepsilon_{xy}$  around the direction transversal to deformation (table 1), in descending order.

Our results (table 1) indicate that the maximum finite strain occurs in the lower flow fronts of region 3, whereas the minimum finite strain occurs in the lobes in zone 4. Strain directions (deformation axis) are not aligned with current day topographic gradients. In particular, lobe deformation axis is oriented  
555  $\sim 40^\circ$  counterclockwise from the topographic slope. Because lobes deform in the direction of the downslope stress, the orientation of the slope at the time of lobe formation must have been different.

Region 4 (the lowest terrace in the northern deposit) deserves a mention. In  
560 region 3, we can observe how the axis of deformation slightly curves towards  
the west. Lobes in region 4 curve westwards and then eastwards, suggesting  
a compression following extensional deformation. This strain pattern agrees  
with previous interpretations of LDA evolution in the region, reflecting the  
past confluence of the south flowing deposit with the north flowing deposit in  
565 the northern and southern walls of Reul Vallis [15]. The inner trough (region  
5), seems to have been incised during or after the convergence of both LDAs,  
perhaps by the action of wind funneled in the trough.

The presence of arcuate bands, and the absence of crevasses indicates the  
material has deformed but not failed. This creep requires viscous deformation  
570 with maximum tensile stresses below that of the critical fracture stress of ice.  
Given the frigid surface temperatures of Amazonian Mars, the relatively low  
stresses involved, and the absence of fracture patterns, the rates of deformation  
within this deposit had to be exceedingly low, implying that deformation was  
likely ongoing for a very long time span. However, a key unresolved matter  
575 is the rheology of cold ice under small stresses over very long periods of time  
[e.g., 76, 6]. Without further understanding of the rheology dynamics under low  
stresses it is not possible to reliably quantify the timespan of activity of this  
deposit. If viscosity was roughly known, this timespan could be estimated from  
equation 5 and observations in table 4.2.

580 Based on our observations, we suggest the following evolution for this LDA.  
First, the deposit originated through cycles of accumulation (snowfall) and com-  
paction, sediment and dust deposition (i.e., dust), and ablation through subli-  
mation. A continuous icy deposit likely covered a good portion of Reull Vallis'  
cross-section, based on the existence of deposits both in the southern and north-  
585 ern wall, the presence of multiple LVF and LDAs within Reull, and the unlikely  
deposition of ice only on canyon walls. After the emplacement, ice ablation ex-  
humed the canyon walls and separated the deposit into northern and southern  
components. Episodes of accumulation and ablation, as well as warm spells oc-  
curring after this point likely enhanced deformation in the north and south ice

590 deposits, triggering glacial creep in the form of lobes, and buttressing (compression) upon collision of the north and south deposit's lower layers, as reflected in the complex deformation axis of zone 4.

Mass balance variability at long timescales - possibly obliquity driven - combined with slow glacial deformation and debris covering triggered the formation  
595 of arcuate MBDB patterns in at least three distinct events, defined by distinct zones in figure 5 separated by flow fronts. In the current mid-latitude interglacial period, decreased temperatures slowed ice creep to a negligible rate, whereas wind erosion continued carving Reull Vallis' current cross-sectional topography, including the inner trough (region 5). Deposit deflation occurred  
600 after deformation, setting the current day slopes which do not coincide with the axis of deformation. The final morphology of the deposit therefore reflects the history of ice accumulation, wind ablation, and ice deformation; whereas the banding patterns likely reflect the mass-balance history of ice deposition and its posterior deformation.

## 605 **5. Conclusions**

In this paper, we use CaSSIS image cube MY34\_005511.224 and derived Color Band Ratio Composites (CBRC), integrated with topographic (MOLA and CTX DEMs) and SHARAD data, to investigate the origin and morphology of a Lobate Debris Apron (LDA) located inside lower Reull Vallis. The LDA  
610 extends from the northern wall towards the bottom of Reull Vallis, and continues with more subdued morphology in the south. Integrated analysis of CaSSIS BLU and CBRC shows that ice is not currently present in relevant concentrations on the surface, whereas SHARAD data yields inconclusive subsurface observations due to the presence of surface clutter returns. Morphological analysis of this site,  
615 previous work, and the presence of multiple ice bodies in the region of eastern Hellas and Reull Vallis strongly support that ice deformation is involved in the formation and evolution of this deposit. We use image and topographic data to reconstruct the deformational history of this deposit and interrogate its interior

structure.

620 We characterize the deformation patterns of this deposit in terms of three scales: distance between deformation fronts or terraces ( $\Delta x$ ), inter-lobe spacing ( $\lambda$ ), and width of the arcuate banding patterns found inside the lobes ( $\gamma$ ). We use spectral analysis to quantify the characteristic wavelengths for arcuate band width and inter-lobe spacing, and measure the distance between terraces from 625 topographic data. The finite strain measurements and the deviation between the deformation axis of the lobes compared with current surface topographic gradients show that the deposit major flow events responded to a past ice thickness and climate conditions. Regularly spaced lobes reflect in their wavelength the basal topographic characteristics of the source region.

630 Arcuate bands, displaying alternating high and low reflectance in CaSSIS data, are interpreted to be Mass-balance Driven Banding (MBDB), and are particularly similar to Arcuate Surface Discontinuities observed in cold-based Antarctic glaciers. The identification of arcuate bands as MBDB opens the door to linking changing environmental conditions with the surface morphology 635 of viscous flow features on Mars similarly to band ogives on Earth, making VFFs valuable time capsules of the recent mid-latitude climate record.

#### *Acknowledgments*

A. Grau Galofre was funded through the Exploration Fellowship program, School of Earth and Space Exploration at Arizona State University, and through 640 the Marie Skłodowska-Curie Action H2020-MSCA-IF-2020: MGFR-101027900. Susan J. Conway was funded through the Centre National d'Études Spatiales (CNES). CaSSIS is a project of the University of Bern funded through the Swiss Space Office via ESA's PRODEX programme. CaSSIS data is being currently released to PSA The instrument hardware development was also supported by 645 the Italian Space Agency (ASI) (ASI-INAF agreement no.I/018/12/0), INAF/Astronomical Observatory of Padova, and the Space Research Center (CBK) in Warsaw. Support from SGF (Budapest), the University of Arizona (Lunar and Planetary Lab.), NASA, and the UK Space Agency (grant ST/R003025/1) are

also gratefully acknowledged. We also acknowledge the financial support from  
650 Région Pays de la Loire, project étoiles montantes METAFLOWS (convention  
N° 2019-14294). The authors express their gratitude to the research groups led  
by professors Kelin X. Whipple and Philip R. Christensen for guidance and in-  
sightful discussions. The authors would also like to thank Michael Christoffersen  
for the help and guidance provided with SHARAD data processing, Erik Young  
655 for insightful discussions on glacial deformation, and two anonymous reviewers  
for their careful consideration and helpful suggestions.

#### *Author contributions*

The authors contributed in the following ways. A. Grau Galofre: Concep-  
tualization; Formal analysis; Funding acquisition; Investigation; Methodology;  
660 Validation; Visualization; Roles/Writing - original draft; Writing - review and  
editing. J. K. Serla: Formal analysis; Investigation; Validation; Roles/Writing -  
original draft; Writing - review and editing. P. Becerra: Formal analysis; Data  
curation; Resources; Validation; Visualization. A. Noblet: Methodology; Re-  
sources; Validation; Visualization. S. J. Conway: Writing - review and editing;  
665 Validation; Visualization.

#### *Competing Interests*

The authors declare they have no competing interests.

#### **References**

- [1] J. W. Head, A. L. Nahm, D. R. Marchant, G. Neukum, Modification of the  
670 dichotomy boundary on Mars by Amazonian mid-latitude regional glacia-  
tion, *Geophysical Research Letters* 33 (8) (2006).
- [2] J. L. Dickson, J. W. Head, C. I. Fassett, Patterns of accumulation and flow  
of ice in the mid-latitudes of Mars during the Amazonian, *Icarus* 219 (2)  
(2012) 723–732.

- 675 [3] J. S. Levy, C. I. Fassett, J. W. Head, Enhanced erosion rates on Mars during Amazonian glaciation, *Icarus* 264 (2016) 213–219.
- [4] E. Hauber, S. van Gasselt, M. G. Chapman, G. Neukum, Geomorphic evidence for former lobate debris aprons at low latitudes on Mars: Indicators of the Martian paleoclimate, *Journal of Geophysical Research: Planets* 113 (E2) (2008).  
680
- [5] I. B. Smith, P. O. Hayne, S. Byrne, P. Becerra, M. Kahre, W. Calvin, C. Hvidberg, S. Milkovich, P. Buhler, M. Landis, et al., The Holy Grail: A road map for unlocking the climate record stored within Mars polar layered deposits, *Planetary and space science* 184 (2020) 104841.
- 685 [6] K. M. Cuffey, W. S. B. Paterson, *The physics of glaciers*, Academic Press, Amsterdam, 2010.
- [7] F. E. Butcher, M. R. Balme, C. Gallagher, N. S. Arnold, S. J. Conway, A. Hagermann, S. R. Lewis, Recent basal melting of a mid-latitude glacier on Mars, *Journal of Geophysical Research: Planets* 122 (12) (2017) 2445–  
690 2468.
- [8] C. Souness, B. Hubbard, R. E. Milliken, D. Quincey, An inventory and population-scale analysis of martian glacier-like forms, *Icarus* 217 (1) (2012) 243–255.
- [9] W. K. Hartmann, T. Thorsteinsson, F. Sigurdsson, Martian hillside gullies and Icelandic analogs, *Icarus* 162 (2) (2003) 259–277.  
695
- [10] B. Hubbard, C. Souness, S. Brough, Glacier-like forms on Mars, *The Cryosphere* 8 (6) (2014) 2047–2061.
- [11] A. Hepburn, F. Ng, S. Livingstone, T. Holt, B. Hubbard, Polyphase mid-latitude glaciation on Mars: Chronology of the formation of superposed  
700 glacier-like forms from crater-count dating, *Journal of Geophysical Research: Planets* 125 (2) (2020) e2019JE006102.

- [12] S. W. Squyres, The distribution of lobate debris aprons and similar flows on Mars, *Journal of Geophysical Research: Solid Earth* 84 (B14) (1979) 8087–8096.
- 705 [13] J. J. Plaut, A. Safaeinili, J. W. Holt, R. J. Phillips, J. W. Head, R. Seu, N. E. Putzig, A. Frigeri, Radar evidence for ice in lobate debris aprons in the mid-northern latitudes of Mars, *Geophysical research letters* 36 (2) (2009).
- [14] J. W. Holt, A. Safaeinili, J. J. Plaut, J. W. Head, R. J. Phillips, R. Seu, 710 S. D. Kempf, P. Choudhary, D. A. Young, N. E. Putzig, et al., Radar sounding evidence for buried glaciers in the southern mid-latitudes of Mars, *Science* 322 (5905) (2008) 1235–1238.
- [15] J. S. Levy, C. I. Fassett, J. W. Head, C. Schwartz, J. L. Watters, Se- 715 questered glacial ice contribution to the global Martian water budget: Geometric constraints on the volume of remnant, midlatitude debris-covered glaciers, *Journal of Geophysical Research: Planets* 119 (10) (2014) 2188–2196.
- [16] S. W. Squyres, Martian fretted terrain: Flow of erosional debris, *Icarus* 34 (3) (1978) 600–613.
- 720 [17] R. P. Sharp, Mars: Fretted and chaotic terrains, *Journal of geophysical research* 78 (20) (1973) 4073–4083.
- [18] D. C. Berman, D. A. Crown, E. C. Joseph, Formation and mantling ages of lobate debris aprons on Mars: Insights from categorized crater counts, *Planetary and Space Science* 111 (2015) 83–99.
- 725 [19] D. C. Berman, F. C. Chuang, I. B. Smith, D. A. Crown, Ice-rich landforms of the southern mid-latitudes of Mars: A case study in Nereidum Montes, *Icarus* 355 (2021) 114170.

- [20] E. I. Petersen, J. S. Levy, J. W. Holt, C. M. Stuurman, New insights into ice accumulation at Galena Creek Rock Glacier from radar imaging of its internal structure, *Journal of Glaciology* 66 (255) (2020) 1–10.
- 730 [21] N. Thomas, G. Cremonese, R. Ziethe, M. Gerber, M. Brändli, G. Bruno, M. Erismann, L. Gambicorti, T. Gerber, K. Ghose, et al., The colour and stereo surface imaging system (CaSSIS) for the ExoMars trace gas orbiter, *Space science reviews* 212 (3) (2017) 1897–1944.
- 735 [22] L. L. Tornabene, F. P. Seelos, A. Pommerol, N. Thomas, C. M. Caudill, P. Becerra, J. C. Bridges, S. Byrne, M. Cardinale, M. Chojnacki, et al., Image simulation and assessment of the colour and spatial capabilities of the Colour and Stereo Surface Imaging System (CaSSIS) on the ExoMars Trace Gas Orbiter, *Space science reviews* 214 (1) (2018) 1–61.
- 740 [23] M. T. Zuber, D. Smith, S. Solomon, D. Muhleman, J. Head, J. Garvin, J. Abshire, J. Bufton, The Mars Observer Laser Altimeter investigation, *Journal of Geophysical Research: Planets* 97 (E5) (1992) 7781–7797.
- [24] R. Jaumann, G. Neukum, T. Behnke, T. C. Duxbury, K. Eichertopf, J. Flohrer, S. Gasselt, B. Giese, K. Gwinner, E. Hauber, et al., The high-resolution stereo camera (HRSC) experiment on Mars Express: Instrument aspects and experiment conduct from interplanetary cruise through the nominal mission, *Planetary and Space Science* 55 (7-8) (2007) 928–952.
- 745 [25] M. C. Malin, J. F. Bell, B. A. Cantor, M. A. Caplinger, W. M. Calvin, R. T. Clancy, K. S. Edgett, L. Edwards, R. M. Haberle, P. B. James, et al., Context camera investigation on board the Mars Reconnaissance Orbiter, *Journal of Geophysical Research: Planets* 112 (E5) (2007).
- 750 [26] A. S. McEwen, E. M. Eliason, J. W. Bergstrom, N. T. Bridges, C. J. Hansen, W. A. Delamere, J. A. Grant, V. C. Gulick, K. E. Herkenhoff, L. Keszthelyi, et al., Mars reconnaissance orbiter’s high resolution imaging science experiment (HiRISE), *Journal of Geophysical Research: Planets* 112 (E5) (2007).
- 755

- [27] R. Seu, R. J. Phillips, D. Biccari, R. Orosei, A. Masdea, G. Picardi, A. Safaeinili, B. A. Campbell, J. J. Plaut, L. Marinangeli, et al., SHARAD sounding radar on the Mars Reconnaissance Orbiter, *Journal of Geophysical Research: Planets* 112 (E5) (2007).  
760
- [28] D. A. Crown, K. H. Price, R. Greeley, Geologic evolution of the east rim of the Hellas basin Mars, *Icarus* 100 (1) (1992) 1–25.
- [29] S. C. Mest, D. A. Crown, Geology of the Reull Vallis region, Mars, *Icarus* 153 (1) (2001) 89–110.
- [30] T. L. Pierce, D. A. Crown, Morphologic and topographic analyses of debris aprons in the eastern Hellas region, Mars, *Icarus* 163 (1) (2003) 46–65.  
765
- [31] D. A. Crown, L. F. Bleamaster, S. C. Mest, Styles and timing of volatile-driven activity in the eastern Hellas region of Mars, *Journal of Geophysical Research: Planets* 110 (E12) (2005).
- [32] M. Ivanov, J. Korteniemi, V.-P. Kostama, M. Aittola, J. Raitala, M. Glamoclija, L. Marinangeli, G. Neukum, Major episodes of the hydrologic history in the region of Hesperia Planum, Mars, *Journal of Geophysical Research: Planets* 110 (E12) (2005).  
770
- [33] V.-P. Kostama, M. Ivanov, A. Polit, T. Törmänen, E. Grosfils, J. Raitala, G. Neukum, Topographic and morphologic characteristics of Reull Vallis, Mars: Implications for the history of the Reull Vallis fluvial system, *Journal of Geophysical Research: Planets* 112 (E11) (2007).  
775
- [34] S. C. Mest, D. A. Crown, et al., Geologic map of MTM-40252 and-40257 quadrangles, Reull Vallis region of Mars, US Department of the Interior, US Geological Survey, 2002.  
780
- [35] D. Crown, T. Pierce, S. McElfresh, S. Mest, Debris aprons in the eastern Hellas region of Mars: Implications for styles and rates of highland degradation, in: *Lunar and Planetary Science Conference, 2002*, p. 1642.

- 785 [36] S. Brough, B. Hubbard, A. Hubbard, Area and volume of mid-latitude glacier-like forms on Mars, *Earth and Planetary Science Letters* 507 (2019) 10–20.
- [37] M. H. Carr, The Martian drainage system and the origin of valley networks and fretted channels, *Journal of Geophysical Research: Planets* 100 (E4) (1995) 7479–7507.
- 790 [38] J. Bell III, M. Malin, M. Caplinger, J. Fahle, M. Wolff, B. Cantor, P. James, T. Ghaemi, L. Posiolova, M. Ravine, et al., Calibration and performance of the Mars reconnaissance orbiter context camera (CTX), *International Journal of Mars Science and Exploration* 8 (2013) 1–14.
- [39] T. Appéré, B. Schmitt, Y. Langevin, S. Douté, A. Pommerol, F. Forget, 795 A. Spiga, B. Gondet, J.-P. Bibring, Winter and spring evolution of northern seasonal deposits on Mars from OMEGA on Mars Express, *Journal of Geophysical Research: Planets* 116 (E5) (2011).
- [40] P. Choudhary, J. W. Holt, S. D. Kempf, Surface clutter and echo location analysis for the interpretation of SHARAD data from Mars, *IEEE* 800 *Geoscience and Remote Sensing Letters* 13 (9) (2016) 1285–1289.
- [41] R. Fergason, T. Hare, J. Laura, HRSC and MOLA blended digital elevation model at 200m v2, astrogeology PDS annex, US Geological Survey. [http://bit.ly/HRSC\\_MOLA\\_Blend\\_v0](http://bit.ly/HRSC_MOLA_Blend_v0) (2018).
- [42] G. A. Neumann, J. B. Abshire, O. Aharonson, J. B. Garvin, X. Sun, 805 M. T. Zuber, Mars Orbiter Laser Altimeter pulse width measurements and footprint-scale roughness, *Geophysical research letters* 30 (11) (2003).
- [43] R. L. Kirk, E. Howington-Kraus, M. R. Rosiek, J. A. Anderson, B. A. Archinal, K. J. Becker, D. Cook, D. M. Galuszka, P. E. Geissler, T. M. Hare, et al., Ultrahigh resolution topographic mapping of Mars with MRO 810 HiRISE stereo images: Meter-scale slopes of candidate Phoenix landing sites, *Journal of Geophysical Research: Planets* 113 (E3) (2008).

- [44] A. Cook, J. Oberst, T. Roatsch, R. Jaumann, C. Acton, Clementine imagery: selenographic coverage for cartographic and scientific use, *Planetary and space science* 44 (10) (1996) 1135–1148.
- 815 [45] R. L. Kirk, E. Howington-Kraus, B. Redding, D. Galuszka, T. M. Hare, B. A. Archinal, L. A. Soderblom, J. M. Barrett, High-resolution topomapping of candidate MER landing sites with Mars Orbiter Camera narrow-angle images, *Journal of Geophysical Research: Planets* 108 (E12) (2003).
- [46] T. N. Titus, H. H. Kieffer, P. R. Christensen, Exposed water ice discovered  
820 near the south pole of Mars, *Science* 299 (5609) (2003) 1048–1051.
- [47] N. E. Putzig, M. T. Mellon, Apparent thermal inertia and the surface heterogeneity of Mars, *Icarus* 191 (1) (2007) 68–94.
- [48] G. Morgan, N. Putzig, M. Perry, H. Sizemore, A. Bramson, E. Petersen, Z. Bain, D. Baker, M. Mastrogiuseppe, R. Hoover, et al., Availability of  
825 subsurface water-ice resources in the northern mid-latitudes of Mars, *Nature Astronomy* 5 (3) (2021) 230–236.
- [49] N. Mangold, P. Allemand, Topographic analysis of features related to ice on Mars, *Geophysical Research Letters* 28 (3) (2001) 407–410.
- [50] N. Mangold, Geomorphic analysis of lobate debris aprons on Mars at Mars  
830 Orbiter Camera scale: Evidence for ice sublimation initiated by fractures, *Journal of Geophysical Research: Planets* 108 (E4) (2003).
- [51] B. Goodsell, M. J. Hambrey, N. F. Glasser, Formation of band ogives and associated structures at Bas Glacier d’Arolla, Valais, Switzerland, *Journal of Glaciology* 48 (161) (2002) 287–300.
- 835 [52] N. Putzig, R. Phillips, B. Campbell, J. Plaut, J. Holt, F. Bernardini, A. Egan, I. Smith, Custom SHARAD processing via the CO-SHARPS processing boutique, in: *Lunar and Planetary Science Conference*, no. 1903, 2016, p. 3010.

- [53] J. F. Nye, A theory of wave formation in glaciers, *Physics of the Movement of Ice*. IAHS Publications 47 (1958) 139–154.  
840
- [54] S. L. Mackay, D. R. Marchant, Obliquity-paced climate change recorded in Antarctic debris-covered glaciers, *Nature communications* 8 (1) (2017) 1–12.
- [55] J. S. Levy, C. I. Fassett, J. W. Holt, R. Parsons, W. Cipolli, T. A. Goudge, M. Tebolt, L. Kuentz, J. Johnson, F. Ishraque, et al., Surface boulder banding indicates Martian debris-covered glaciers formed over multiple glaciations, *Proceedings of the National Academy of Sciences* 118 (4) (2021) e2015971118.  
845
- [56] M. Hambrey, Foliation, minor folds and strain in glacier ice, *Tectonophysics* 39 (1-3) (1977) 397–416.  
850
- [57] M. J. Hambrey, W. Lawson, Structural styles and deformation fields in glaciers: a review, *Geological Society, London, Special Publications* 176 (1) (2000) 59–83.
- [58] P. J. Hudleston, R. L. Hooke, Cumulative deformation in the Barnes Ice Cap and implications for the development of foliation, *Tectonophysics* 66 (1-3) (1980) 127–146.  
855
- [59] N. Matsuoka, Solifluction rates, processes and landforms: a global review, *Earth-Science Reviews* 55 (1-2) (2001) 107–134.
- [60] J. Rowland, C. Jones, G. Altmann, R. Bryan, B. Crosby, L. Hinzman, D. Kane, D. Lawrence, A. Mancino, P. Marsh, et al., Arctic landscapes in transition: responses to thawing permafrost, *Eos, Transactions American Geophysical Union* 91 (26) (2010) 229–230.  
860
- [61] A. Johnsson, D. Reiss, E. Hauber, M. Zanetti, H. Hiesinger, L. Johansson, M. Olvmo, Periglacial mass-wasting landforms on Mars suggestive of transient liquid water in the recent past: Insights from solifluction lobes on Svalbard, *Icarus* 218 (1) (2012) 489–505.  
865

- [62] R. C. Glade, M. M. Fratkin, M. Pouragha, A. Seiphoori, J. C. Rowland, Arctic soil patterns analogous to fluid instabilities, *Proceedings of the National Academy of Sciences* 118 (21) (2021).
- 870 [63] D. J. Milton, Water and processes of degradation in the martian landscape, *Journal of Geophysical Research* 78 (20) (1973) 4037–4047.
- [64] H. E. Huppert, Flow and instability of a viscous current down a slope, *Nature* 300 (5891) (1982) 427–429.
- [65] S. Troian, E. Herbolzheimer, S. Safran, J. Joanny, Fingering instabilities  
875 of driven spreading films, *EPL (Europhysics Letters)* 10 (1) (1989) 25.
- [66] J. R. de Bruyn, P. Habdas, S. Kim, Fingering instability of a sheet of yield-stress fluid, *Physical Review E* 66 (3) (2002) 031504.
- [67] D. M. Baker, L. M. Carter, Probing supraglacial debris on Mars 1: Sources, thickness, and stratigraphy, *Icarus* 319 (2019) 745–769.
- 880 [68] J. Nye, W. Durham, P. Schenk, J. Moore, The instability of a south polar cap on Mars composed of carbon dioxide, *Icarus* 144 (2) (2000) 449–455.
- [69] S. Byrne, The polar deposits of Mars, *Annual Review of Earth and Planetary Sciences* 37 (2009).
- [70] P. L. Moore, Deformation of debris-ice mixtures, *Reviews of Geophysics*  
885 52 (3) (2014) 435–467.
- [71] P. J. Hudleston, Structures and fabrics in glacial ice: A review, *Journal of Structural Geology* 81 (2015) 1–27.
- [72] E. Waddington, Wave ogives, *Journal of Glaciology* 32 (112) (1986) 325–334.
- 890 [73] Á. Ignéczi, A. J. Sole, S. J. Livingstone, F. S. Ng, K. Yang, Greenland Ice Sheet surface topography and drainage structure controlled by the transfer of basal variability, *Frontiers in Earth Science* 6 (2018) 101.

- [74] C. Vincent, M. Dumont, D. Six, F. Brun, G. Picard, L. Arnaud, Why do the dark and light ogives of Forbes bands have similar surface mass balances?,  
895 Journal of Glaciology 64 (244) (2018) 236–246.
- [75] S. J. Jennings, M. J. Hambrey, et al., Structures and Deformation in Glaciers and Ice Sheets, Reviews of Geophysics 59 (3) (2021) e2021RG000743.
- [76] R. Greve, Fluid dynamics of planetary ices, GAMM-Mitteilungen 29 (1)  
900 (2006) 29–51.